Dalton Transactions

Accepted Manuscript

ROYAL SOCIETY OF CHEMISTRY

www.rsc.org/dalton

Crystal Chemistry and Luminescent Properties of Red-Emitting $CsGd_{1-x}Eu_x(MoO_4)_2$ Solid-Solution Phosphors

Pinglu Shi[1], Zhiguo Xia[1,2*], Maxim S. Molokeev[3], Victor V. Atuchin[4,5,6]

Crystal structure and red-emitting luminescence properties of scheelite related $CsGd_{1-x}Eu_x(MoO_4)_2$ solid-solution phosphors have been investigated.

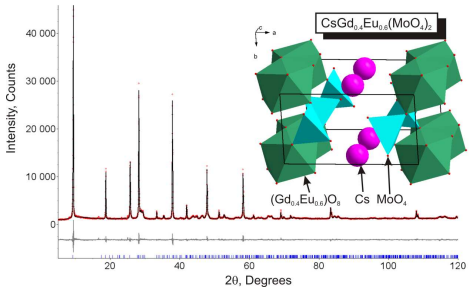

Crystal Chemistry and Luminescent Properties of Red-Emitting $CsGd_{1-x}Eu_x(MoO_4)_2$ Solid-Solution Phosphors

Pinglu Shi[1], Zhiguo Xia[1,2*], Maxim S. Molokeev[3], Victor V. Atuchin[4,5,6]

[1]*School of Materials Sciences and Technology, China University of Geosciences, Beijing 100083, China*

[2]*School of Materials Sciences and Engineering, University of Science and Technology Beijing, Beijing 100083, China*

[3]*Laboratory of Crystal Physics, Institute of Physics, SB RAS, Krasnoyarsk 660036, Russia*

[4]*Laboratory of Optical Materials and Structures, Institute of Semiconductor Physics, SB RAS, Novosibirsk 630090, Russia*

[5]*Functional Electronics Laboratory, Tomsk State University, Tomsk 634050, Russia*

[6] *Laboratory of Semiconductor and Dielectric Materials, Novosibirsk State University, Novosibirsk 630090, Russia*

[*] Author to whom correspondence should be addressed:

Zhiguo Xia (xiazg@cugb.edu.cn)

Tel.: +86-10-8237-7955; Fax.: +86-10-8237-7955

†Electronic supplementary information (ESI) available. See DOI:xxx

Abstract: Scheelite related alkali-metal rare-earth double molybdate compounds with the general formula of $ALn(MoO_4)_2$ can find a wide application in red phosphors. Crystal chemistry and luminescent properties of red-emitting $CsGd_{1-x}Eu_x(MoO_4)_2$ solid-solution phosphors have been evaluated in the present paper. A detailed analysis of the structural properties indicates the formation of iso-structural scheelite-type $CsGd_{1-x}Eu_x(MoO_4)_2$ solid-solutions over the composition range of $0 \leq x \leq 1$. The photoluminescence emission (PL) and excitation (PLE) spectra, and the decay curves were measured for this series of compounds. The critical doping concentration of Eu^{3+} is determined to be $x = 0.6$ in order to realize the maxim emission intensity. The emission spectra of as-obtained $CsGd_{(1-x)}Eu_x(MoO_4)_2$ phosphors are shown with narrow high intensity red lines at 592 and 615 nm upon excitation at 394 or 465 nm with a revealing great potential for the applications in white light-emitting diodes devices.

1. Introduction

White light-emitting diodes (LEDs) are promising to become the next generation of solid-state illumination lighting due to their unique properties, such as high reliability, long lifetime, low energy consumption and environmental friendliness, and so on.[1-3] Commonly, the most convenient way to generate white light is the combination of an InGaN-based blue LED chip with broad-band yellow phosphor $Y_3Al_5O_{12}:Ce^{3+}$. Nevertheless, one of the challenges, though, is that this method comes from the low color-rendering index (CRI) of the emitter due to the deficiency of red emission from $Y_3Al_5O_{12}:Ce^{3+}$phosphor.[4] In order to overcome this shortcoming, high-efficient red-emitting phosphor is essential. Therefore, much attention has been paid to Eu^{3+}-activated scheelite-related alkali-metal rare-earth double molybdates and tungstates with the general formula of $ALn(MO_4)_2$ (A is an alkali-metal cation or Tl^+ , Ag^+, Cu^+), Ln is a rare earth metal cation or Y^{3+} and M is Mo^{6+} or W^{6+}), owing to their good optical properties, stability and a relatively simple preparation. Accordingly, many double molybdate- and tungstate-based phosphors have been investigated, such as $NaY(MoO_4)_2:Eu^{3+}$,[5] $NaEu_{0.96}Sm_{0.04}(MoO_4)_2$,[6] $NaLa(MoO_4)_2:Eu^{3+}$,[7] $KEu(MoO_4)_2$,[8] $NaLu(WO_4)_2:Eu^{3+}$,[9] and so on. The compounds of series $ALn(MO_4)_2$ possess different crystal structures depending on a specific cation combination.[10-18] As for such a host lattice, all the

rare earth ions occupy the low symmetry sites surrounded by oxygen atoms. When the special red-emitting rare earth ions, such as Eu^{3+}, Sm^{3+} or Pr^{3+}, are introduced to the host, the doping ions insert into the existing Ln^{3+} sites. However, the Ln^{3+} sites are of low symmetry, and, as a result, these compounds doped with Eu^{3+} can show the strong red emission arised from transition $^5D_0$-$^7F_2$ at nearly 613 nm. Besides, these phosphors exhibit intense absorption at 394 and 465 nm, which well meets the application for the near-UV/blue LED chip.

Since Cs^+ has the largest effective ion radius in the alkali-metal group, it is expected to obtain the new red-emitting phosphors with high-efficiency and high quenching concentration in the $CsLn(MO_4)_2$ compounds. Regrettably, the $CsLn(MO_4)_2$ compounds are poorly investigated, and even structural information has been reported only for several crystals.[19-23] In this study, $CsGd_{1-x}Eu_x(MoO_4)_2$ solid-solution phosphors are proposed and designed, and the crystal chemistry and luminescent properties of red-emitting $CsGd_{1-x}Eu_x(MoO_4)_2$ phosphors are evaluated in details. The effective radii of Gd^{3+} and Eu^{3+} ions are very close and, respectively, continuous tuning of structural and spectroscopic parameters can be reasonably supposed in quasi-binary system $CsGd(MoO_4)_2$ - $CsEu(MoO_4)_2$. It should be noticed, however, that the existence of $CsGd(MoO_4)_2$ molybdate has long been known, and some thermal and magnetic properties were observed in several studies.[24-27] Contrary

to that, the properties of $CsEu(MoO_4)_2$ are unknown in the literature.

2. Experimental

A series of $CsGd_{1-x}Eu_x(MoO_4)_2$ (x = 0, 0.05, 0.1, 0.2, 0.4, 0.6, 0.8, 1.0) samples was synthesized using the conventional solid-state reactions. The starting materials, Cs_2CO_3(99.9%), Gd_2O_3 (99.99%), MoO_3(99.95%) and Eu_2O_3(99.99%) were weighed on stoichiometric ratio and mixed homogeneously in an agate mortar. The 0.5% excess of Cs_2CO_3 was added to be used as a self-flux. After grindings, the mixtures were being calcined in the air at 950^{o}C for 6 h in a muffle furnace to form the final product.[28] Subsequently, the as-obtained samples were ground into powders, and the phase composition was controlled.

The X-ray powder diffraction (XRD) data were collected on a SHIMADZU model XRD-6000 diffractometer equipped with a linear detector and Cu-Kα radiation (λ= 0.15406 nm) source operating at 40 kV and 30 mA. The photoluminescence emission (PL) and excitation (PLE) spectra were measured using a Hitachi F-4600 spectrometer with a 150 W Xe lamp as the excitation source under the working voltage of 500 V. The luminescence decay curves were recorded on a spectrofluorometer (HORIBA, JOBIN YVON FL3- 21), and the 460 nm pulse laser radiation (nano-LED) was used as the excitation source.[29] The

temperature-dependence luminescence properties were measured on the same spectrophotometer, which was combined with a self-made heating attachment and a computer-controlled electrical furnace.

3. Results and discussions

The XRD patterns of $CsGd_{1-x}Eu_x(MoO_4)_2$ (x = 0, 0.05, 0.1, 0.2, 0.4, 0.6, 0.8, 1.0) are displayed in Figure 1. All the samples with different Gd/Eu contents represent similar diffraction patterns without impurity peaks. All diffraction peaks are indexed by a single monoclinic phase, and the peak positions agree well with JCPDS card 41-419 $CsGd(MoO_4)_2$.[30] Considering the ion sizes and valence states, Eu^{3+} ions are most likely to occupy the Gd^{3+} sites. The structure of $CsGd_{1-x}Eu_x(MoO_4)_2$ is isotructural to $CsDy(MoO_4)_2$, and we use the atomic coordinates to refine the structure of the series of $CsGd_{1-x}Eu_x(MoO_4)_2$ solid solutions. All refinements and data processing were performed using the program TOPAS 4.2. The concentration of Gd was not refined because Gd^{3+} and Eu^{3+} ions have similar atomic scattering functions, and, therefore, the *x* values were constrained in accordance to nominal compositions. All metal atoms were refined with isotropic thermal parameters. One thermal parameter, however, was refined for all oxygen atoms. Correction for the preferred orientation was implemented on the (100) plane. The refinement was stable and gave

low R-factors. The main parameters of processing and refinement are summarized in Table 1. As an example, the experimental (dots) and theoretical (lines) X-ray diffraction patterns of $CsGd_{0.4}Eu_{0.6}(MoO_4)_2$ are shown in Figure 2. The crystal structure is illustrated in the inset in Figure 2. The $CsGd_{1-x}Eu_x(MoO_4)_2$, $0 \le x \le 1$ solid solutions crystallize in space group $P2/c$ exhibiting a layered structure. The stacking of alternating layers: –Gd – (MoO_4) – Cs – (MoO_4) – runs along the crystallographic a axis. Each layer is parallel to the (100) cleavage plane. All the rare earth ions and Cs^+ ions are located in the eight-coordinated sites surrounded by oxygen atoms. The dependencies of unit cell parameters on x are shown in Figures 1S-4S. The dependence of unit cell volume V on x in $CsGd_{1-x}Eu_x(MoO_4)_2$ is shown in Figure 3. It is found that the $CsGd_{1-x}Eu_x(MoO_4)_2$ compounds are isostructural with the random substitution of Gd/Eu atoms in the same Ln^{3+} sites. Furthermore, the atom coordinates and thermal parameters, as well as the main bond-lengths of the $CsGd_{1-x}Eu_x(MoO_4)_2$ solid-solution compounds are listed in Table S1 and Table S2.

Based on the Rietveld refinement results, the unit cell volume is proportional to value x, which also verified that the solutions are isostructural and obey the Vegard's rule. As it is evident from Figures 1S and 2S, the variations of cell parameters a and b are relatively small. Comparatively to that, the drastic increase of parameter c takes place on substitution of Gd^{3+} by Eu^{3+} ions as shown in Figure 3S. Monoclinic angle β

decreases with the increase of *x* and remains to be close to 90° (Fig. 4S). Thus, it can be concluded that the increase of *V* in $CsGd_{1-x}Eu_x(MoO_4)_2$ solid solutions is provided dominantly by unit cell elongation parallel to axis *c*. It is interesting to consider a possible atomic mechanism of such strongly anisotropic variation of the structural parameters. The effective ionic radius of Eu^{3+} is a little bigger that that of Gd^{3+} ion in octupole coordination.[31] Respectively, the averaged dimentions of $(Gd,Eu)O_8$ square antiprisms should increase with the increase of *x*. In the *a* and *b* directions, this general intumescences of the $(Gd,Eu)O_8$ square antiprisms can be partly damped through deformation and rotation of other metal polyhedra, and that results in a little variation of cell parameters *a* and *b*. In *c* directions, however, the $(Gd,Eu)O_8$ square antiprisms are strictly linked by edges into chains and the damping is impossible. Then, the variation of $(Gd,Eu)O_8$ square antiprisms with the increase of *x* is transmitted to the increase of parameter *c*.

It is known from available structural information that compounds $ALn(MoO_4)_2$ (A=Li, Na, Ag, Cu, K, Cs, Rb, Tl) may crystallize in different space groups of *P*2/*c* to *Pccm*, *Pbcn* and $I4_1/a$.[30] Recently, it has been found that $ALn(MoO_4)_2$ molybdates can be classified using quite simple parameter $p = R_{Ln}/R_A$, where R_{Ln} - radius of Ln^{3+} ion, R_A - radius of A ion.[17] The related diagram is shown in Figure 4. In the considered molybdates $CsGd_{1-x}Eu_x(MoO_4)_2$, parameter *p* increases in the

range of 1.632-1.652 on increase *x*, and, therefore, the compounds appeared close to the border between the sectors of *P*2/*c* and *Pccm* space groups. It is very interesting because the local symmetry of Ln site in *P*2/*c* is 2, but the local symmetry of Ln site in *Pccm* is 222. The structural difference could lead to a difference in physical properties. However, all compounds $CsGd_{1-x}Eu_x(MoO_4)_2$, $0 \le x \le 1$, crystallize in *P*2/*c*. This helps us to define precisely the board in Figure 4 between the sectors related to *P*2/*c* and *Pccm* space groups and noticeably expand the region of *P*2/*c* phases in the diagram.

The developed diagram shown in Figure 4 is valuable for crystal symmetry predictions. For example, the hypothetical solid solutions $CsSm_{1-x}Eu_x(MoO_4)_2$ and $CsPm_{1-x}Eu_x(MoO_4)_2$, containing the Sm^{3+} and Pm^{3+} ions with effective ion radii lower than that of Eu^{3+} with CN = 8, can be considered.[31] Then, in compounds $CsSm_{1-x}Eu_x(MoO_4)_2$ and $CsPm_{1-x}Eu_x(MoO_4)_2$, the value of *p* runs from 1.652 to 1.603 and from 1.652 to 1.592 on decrease *x*, respectively. Thus, in accordance with the diagram shown in Figure 4, the binary molybdates should appear in the sector of space group *Pccm*.

Another interesting subject is a substitution of Mo^{6+} by W^{6+} in binary molybdates because the solutions are promising for the creation of effective red phosphors.[32] As for the tungsten oxides with general composition $CsLn(WO_4)_2$,

only the structure of $CsLu(WO_4)_2$ has been reported on up to now.[33] This compound crystallize in *P2/c* space group, and this feature is similar to the related Cs-containing molybdates. In tungstate $CsLu(WO_4)_2$, however, in comparison with molybdates, the monoclinic angle β is greater and two oxygen ions are pushed closer to tungsten, and that results in the appearance of $[WO_6]$ octahedrons, as shown in Figure 5, instead of MoO_4 tetrahedrons present in molybdates. Another specific feature of $ALn(WO_4)_2$ tungstates is a wide spread of monoclinic crystals with space group *C2/c* even for comparatively small A cations, and that is forbidden in molybdates. Indeed, such well known laser hosts as $KEu(WO_4)_2$,[34] $RbGd(WO_4)_2$,[35] $TlSm(WO_4)_2$,[36] $KGd(WO_4)_2$[37] and others can be considered. So, in spite of Mo^{6+} and W^{6+} ions possess similarly effective ion radii, they show different behavior in binary crystals and structural relations should be specified selectively.

The emission spectra of $CsGd_{1-x}Eu_x(MoO_4)_2$ phosphors in the red spectral range from 580 to 660 nm under excitation at 394 and 465 nm are shown in Figure 6a and 6b, respectively. The insets indicate the trends of emission intensities as a function of the Eu^{3+} concentration. The emission intensities increase with the increasing Eu^{3+} content up to $x = 0.6$ and decreases thereafter. This indicates that the phosphors have a high critical value of Eu^{3+} quenching concentration.[38] The emission spectra exhibit a strong peak centering at 615 nm corresponding to the $^5D_0$-$^7F_2$ electric dipole transition

of Eu^{3+} ions. The weak emission peak around 592 nm is assigned to the magnetic dipole transition of $^5D_0$-$^7F_1$.[7] From the structural analysis, the Eu^{3+} site in the $CsGd(MoO_4)_2$ host lacks of inversion symmetry. According to the Judd-Ofelt theory,[39] in this case the electric dipole emission is strong, and the magnetic dipole transition is relatively weak.[1, 3, 40] Our experimental results also confirm this point. Other emission peaks between 650 and 710 nm corresponding to $^5D_0$-$^7F_3$ and $^5D_0$-$^7F_4$ transitions of Eu^{3+} ion are very weak and can not be clearly observed.

The excitation spectrum monitored at 615 nm, emission spectrum under 394 nm excitation of $CsGd_{0.4}Eu_{0.6}(MoO_4)_2$, and energy level diagram of Eu^{3+} illustrating the two spectra are displayed in Figure 7. The excitation spectrum reveals two regions: the broad absorption band extending from 215 nm to 350 nm with a center at 297 nm and several narrow excitation peaks above 350 nm. The wide excitation band mainly originated from the charge transfer transition of O^{2-}-Mo^{6+} [ligand to metal charge transfer (LMCT)]. Above this, the LMCT of O^{2-}-Eu^{3+} contributed to the band.[41-43] The LMCT band position can be estimated using the empirical formula by Jørgensen:

$$E_{ct}(cm^{-1}) = [\chi_{opt}(X) - \chi_{opt}(M)] \times 30,000\,cm^{-1} \quad (1)$$

where $\chi_{opt}(X)$ is the optical electronegativity of the anion, and the value is equal to Pauling electronegativity 3.2; $\chi_{opt}(M)$ is the optical electronegativity of the central metal ion, with $\chi_{opt}(Mo) = 2.101$ [44] and $\chi_{opt}(Eu) = 1.74$ [42]. From expression (1), the

LMCT of O^{2-}-Mo^{6+} is around ~303 nm and the O^{2-}-Eu^{3+} LMCT is at ~228 nm. Clearly, the estimations well agree to the experimental result. The sharp excitation lines between 350 nm and 550 nm are attributed to the f-f transitions of Eu^{3+}. Moreover, some other tiny excitation peaks were also detected. The excitation spectrum demonstrates that $CsGd_{0.4}Eu_{0.6}(MoO_4)_2$ phosphor can well absorb near-UV/blue light. For the present compound, the intensity of f-f transitions is higher than that of charge transfer transition. Furthermore, the UV-Vis reflectance spectrum of $CsGd_{0.4}Eu_{0.6}(MoO_4)_2$ phosphor was measured, as shown in Fig. 8. The broad band absorption band below 350 nm should be ascribed to the LMCT band. Except for this, several sharp absorption lines corresponding to the f-f transitions of Eu^{3+} ions are detected. Especially, some observed excitation and absorption lines at 394 and 465 nm can echo the efficient absorption meeting the possible application for the near-UV/blue LED chip.

The lifetime of Eu^{3+} $^5D_0$-$^7F_2$ emission was measured at different Eu^{3+} concentrations. The normalized decay curves recorded for the $CsGd_{(1-x)}Eu_x(MoO_4)_2$ phosphors under the excitation at 460 nm are shown Figure 9. They can be well fitted using a first-order exponential decay formula:

$$I(t) = I_0 + A\exp(-t/\tau) \quad (2)$$

where I and I_0 are the luminescence intensity at time t and 0, A is a constant, and τ

represents the characteristic decay time for exponential components.[45] The decay curves indicate that all Eu^{3+} ions occupy the same atom environment, which is consistent with the description of the crystal structure above.[4] On the basis of the results of fitting a single exponential decay, the lifetime values of $CsGd_{1-x}Eu_x(MoO_4)_2$ phosphors were calculated to be 0.579, 0.581, 0.626, 0.633, 0.539 and 0.475 ms at different Eu concentrations. The values of lifetime initially increase and reach the maximum at the Eu^{3+} content equal to 0.6. Then, the values rapidly decrease on the increasing Eu^{3+} content. Obviously, the variation of the luminescence decay curves is the same as that of the emission spectra with the variation of Eu^{3+} concentration. The concentration quenching effect assigned to energy transfer is verified in more details. When Eu^{3+} doping concentration increases from 0.1 to 0.6, more and more luminescence sites in the $CsGd_{1-x}Eu_x(MoO_4)_2$ host are occupied by Eu^{3+}. However, on Eu^{3+} doping above the critical point, the high concentration of Eu^{3+} will enlarge the ratio of ions approaching. As a result, both the energy transfer rate between Eu^{3+} and Eu^{3+} and the probability of energy transfer to the killer site (such as defects) increase. Consequently, the lifetimes are shortened and the emission intensities are decreased as the Eu^{3+} concentration grows.[46]

The thermal stability of phosphor is an important aspect when it is used in high-powered LEDs. The emission spectra measured for $CsGd_{0.4}Eu_{0.6}(MoO_4)_2$ under

394 nm excitation at a different temperature between 25 and 250 ^{o}C are shown in Figure 10. The inset shows the temperature dependence of the luminescence quenching. The emission intensity of the phosphor decreases on the temperature rising up to 250 °C. Obviously, when the temperature increased to 150°C, the corresponding PL intensity dropped to 81.3% of its initial value. The result indicates that phosphor $CsGd_{0.4}Eu_{0.6}(MoO_4)_2$ has a relatively good thermal quenching effect. The thermal quenching phenomenon can be explained using the configurational coordinate diagram. In a high-temperature environment, electron-phonon interaction is dominant. Initially, luminescence center Eu^{3+} in the excited state is activated by phonon interaction and then releases through a crossover between the $^5D_0$ excited state and ^7F_j (j = 1, 2, 3, 4) ground state.[47] Thus, the emission intensity decreases as the temperature rises. In order to make the behavior of thermal quenching clear, the activation energy was calculated through the Arrhenius equation:[48]

$$I_T = \frac{I_0}{1 + c\exp(-\frac{\Delta E}{kT})} \qquad (3)$$

where I_0 and I_T are the luminescence intensities of $CsGd_{0.4}Eu_{0.6}(MoO_4)_2$ at room temperature and at tested temperature, respectively, c is a constant; k is the Boltzmann constant (8.617×10^{-5} eV/K); ΔE is the activation energy for thermal quenching. According to equation (3), the plot of $\ln[(I_0/I_T)-1]$ *vs.* $1/kT$ yields a straight line illustrated in Figure 11, and activation energy ΔE can be obtained from the slope of

the plot. The ΔE value is calculated to be 0.329 eV, and the value is comparatively high.

Figure 12 exhibited the CIE chromaticity coordinate of the phosphor, and the value is (0.665, 0.335), which is located in the deep red region. The color point is near the edge of the CIE diagram, showing that the phosphor has its high color purity.

4. Conclusions

In summary, a series of red-emitting phosphors $CsGd_{(1-x)}Eu_x(MoO_4)_2$ (x = 0, 0.05, 0.1, 0.2, 0.4, 0.6, 0.8, 1.0) were prepared by the conventional solid-state synthesis. The crystal structure of $CsGd(MoO_4)_2$ and $CsEu(MoO_4)_2$ end compounds is defined for the first time. The XRD patterns indicate that the obtained materials crystallize in a layered structure and Eu^{3+} ions enter into the Gd^{3+} sites. The crystal structures of $CsGd_{(1-x)}Eu_x(MoO_4)_2$ solutions were clarified from powder X-ray diffraction data as a function of composition. The luminescence properties of these compounds have been reported. Under the excitation of 394 and 465 nm, the systems show a strong red emission at 615 nm due to the $^5D_0$-$^7F_2$ transition. Both the emission intensities and the lifetimes are changing with the Eu^{3+} content in the host lattice. Besides, the phosphors can efficiently absorb near-UV/blue light, making them candidates as potential red phosphors for near-UV/blue LED applications.

ACKNOWLEDGMENTS

The present work was supported by the National Natural Science Foundations of China (Grant No. No.51002146, No.51272242), Natural Science Foundations of Beijing (2132050), the Program for New Century Excellent Talents in University of Ministry of Education of China (NCET-12-0950), Beijing Nova Program (Z131103000413047), Beijing Youth Excellent Talent Program (YETP0635) and the Funds of the State Key Laboratory of New Ceramics and Fine Processing, Tsinghua University (KF201306). V. V. A. gratefully acknowledge the Ministry of Education and Science of the Russian Federation for the financial support.

REFERENCES

(1) Y. S. Zhang, H. Jiao and Y. R. Du, *J. Lumin.*, 2011, **131**, 861.

(2) Y. Q. Zhou, J. Liu, X. Y. Yang, X. B. Yu and J. Zhuang, *J. Electrochem. Soc.*, 2010, **157**, H278.

(3) J. J. Wierer, J. Y. Tsao and D.S. Sizov, *Laser Photonics Rev.*, 2013, **7**, 963.

(4) L. Zeng and W. J. Tang, *Physica B*, 2011, **406**, 2901.

(5) B. Yan and J. H. Wu, *Mater. Chem. Phys.*, 2009, **116**, 67.

(6) Z. L. Wang, H. B. Liang, L. Y. Zhou, J. Wang, M. L. Gong and Q. Su, *J. Lumin.*, 2008, **128**, 147.

(7) M. Yang, H. P. You, Y. C. Jia, H. Qiao, N. Guo and Y. H. Song, *CrystEngComm*, 2011, **13**, 4046.

(8) T. Wu, Y. F. Liu, Y. N. Lu, L. Wei, H. Gao and H. Chen, *CrystEngComm*, 2013, **15**, 2761.

(9) Z. J. Wang, J. P. Zhong, H. B. Liang and J. Wang, *Opt. Mater. Express*, 2013, **3**, 418.

(10) S. V. Borisov and R. F. Klevtsova, *Kristallografiya*, 1968, **13**, 517.

(11) P. V. Klevtsov and R. F. Klevtsova, *J. Struct. Chem.*, 1977, **18**, 419.

(12) V. V. Atuchin and B. I. Kidyarov, *J. Korean Cryst. Growth Cryst. Technol.*, 2002, **12**, 323.

(13) V. V. Atuchin, O. D. Chimitova, T. A. Gavrilova, M. S. Molokeev, S. J. Kim, N. V. Surovtsev and B. G. Bazarov, *J. Cryst. Growth*, 2011, **318**, 683.

(14) G. Banoît, J. Véronique, A. Arnaud and G. Alain, *Solid State Sci.*, 2011, **13**, 460.

(15) V. V. Atuchin, V. G. Grossman, S. V. Adichtchev, N. V. Surovtsev, T. A. Gavrilova and B. G. Bazarov, *Opt. Mater.*, 2012, **34**, 812.

(16) M. Maczka, A. G. S. Filho, W. Paraguassu, P. T. C. Freire, J. M. Filho and J. Hanuza, *Prog. Mater. Sci.*, 2012, **57**, 1335.

(17) O. D. Chimitova, V. V. Atuchin, B. G. Bazarov, M. S. Molokeev, Bazarova and Zh. G., *Proc. SPIE*, 2013, **8771**, 8771A.

(18) V. V. Atuchin, O. D. Chimitova, S. V. Adichtchev, B. G. Bazarov, T. A. Gavrilova, M. S. Molokeev, N. V. Surovtsev, Bazarova and Zh. G., *Mater. Lett.*, 2013, **106**, 26.

(19) M. V. Bobkova, I. V. Shakhno, V. E. Plyuschev and T.S. Izv. Akad. Balushkina, *Nauk. Khim. Khim. Tekhnol.*, 1971, **14**, 323.

(20) V. A. Vinokurov and P. V. Klevtsov, *Sov. Phys. Crystallogr. (Engl. Transl.)*, 1972, **17**, 127.

(21) R. F. Klevtsova, V. A. Vinokurov and P. V. Klevtsov, *Kristallografiya*, 1972, **17**, 284.

(22) C. C. Torardi, C. Page, L. H. Brixner, G. Blasse and G. J. Dirksen, *J. Solid State Chem.*, 1987, **69**, 171.

(23) E. N. Khatsko, A. Zheludev, J. M. Tranquada, W. T. Klooster, A. M. Knigavko and R. C. Rivastava, *Low Temp. Physics*, 2004, **30**, 184.

(24) N. V. Ivannikova, L. P. Kozeeva and A. A. Pavlyuk, *Inorg. Mater.*, 1988, **24**, 379.

(25) P. Stefányi, A. Feher, A. Orendáčová, E. E. Anders and A. I. Zvyagin, *J. Magn. Magn. Mater.*, 1988, **73**, 129.

(26) A. G. Anders, S. V. Volotskii, S. V. Startsev, A. Feher and A. Orendáčová,

Fizika Nizkikh Temperatur, 1995, **21**, 52.

(27) K. Tibenská, V. Tkác, A. Orendáčová, M. Orendáč, A. Feher, J. Šebek and V. Sechovský, *Acta Phys. Polonica A*, 2010, **18**, 971.

(28) S. Neeraj, N. Kijima and A. K. Cheetham, *Chem. Phys. Lett.*, 2004, **387**, 2.

(29) P. L. Shi and Z. G. Xia, *Mater. Res. Bull.*, 2014, **49**, 589.

(30) ICSD database (ICSD 2013-2, FindIt Version 1.9.3).

(31) R. D. Shannon, *Acta Cryst. A*, 1976, **32**, 751.

(32) V. A. Morozov, A. Bertha, K. Meert. S. Van Rompaey, D. Batuk, G. T. Martinez, S. Van Aert, P. F. Smet, M. V. Raskina, D. Poelman, A. M. Abakumov and J. Hadermann, *Chem. Mater.*, 2013, **24**, 4387.

(33) C. C. Torardi, C. Page, L. H. Brixner, G. Blasse and G. J. Dirksen, *J. Solid State Chem.*, 1987, **69**, 171.

(34) G. -H. Lee and S. Kang, *J. Lumin.*, 2011, **131**, 2606.

(35) K. P. Wang, J. X. Zhang, J. Y. Wang, W. T. Yu, H. J. Zhang, X. P. Wang, Z. P. Wang and M. F. Ba, *J. Crys. Growth*, 2005, **281**, 407.

(36) H. C. Mumm and H. Mueller Buschbaum, *Monatshefte fuer Chemie*, 1987, **118**, 1357.

(37) M. C. Pujol, M. Rico, C. Zaldo, R. Sole, V. Nikolov, X. Solans, M. Aguilo and F. Diaz, *Appl. Phys. B*, 1999**,** 187.

(38) S. H. Park, K. H. Lee, S. Unithrattil, H. S. Yoon, H. G. Jang and W. B. Im, *J. Phys. Chem. C*, 2012, **116**, 26850.

(39) L. Xu, X. Y. Yang, Z. Zhai, X. Chao, Z. H. Zhang and W. H. Hou, *Cryst. Eng.*, 2011, **13**, 4921.

(40) S. Ida, C. Ogata, M. Eguchi, W. J. Youngblood, T. E. Mallouk and Y. Matsumoto, *J. Am. Chem. Soc.*, 2008, **130**, 7052.

(41) K. W. Huang, W. T. Chen, C. I. Chu, S. F. Hu, H. S. Sheu, B. M. Cheng, J. M. Chen and R. S. Liu, *Chem. Mater.*, 2012, **24**, 2220.

(42) X. L. Gao, Y. H. Wang, D. Wang and B. T. Liu, *J. Lumin.*, 2009, **129**, 840.

(43) V. Sivakumar and U. V. Varadarajuz, *J. Electrochem. Soc.*, 2005, **152**, H168.

(44) V. Dimitrov and T. Komatsu, *J. Solid State Chem.*, 2012, **196**, 574.

(45) Z. G. Xia, R. S. Liu, K. W. Huang and V. Drozd, *J. Mater. Chem.*, 2012, **22**, 15183.

(46) D. Y. Wang, C. H. Huang, Y. C. Wu and T. M. Chen, *J. Mater. Chem.*, 2011, **21**, 10818.

(47) G. Y. Lee, J. Y. Han, W. B. Im, S. H. Cheong and D. Y. Jeon, *Inorg. Chem.*, 2012, **51**, 10688.

(48) J. Zhou, Z. G. Xia, M. X. Yang and K. Shen, *J. Mater. Chem.*, 2012, **22**, 21935.

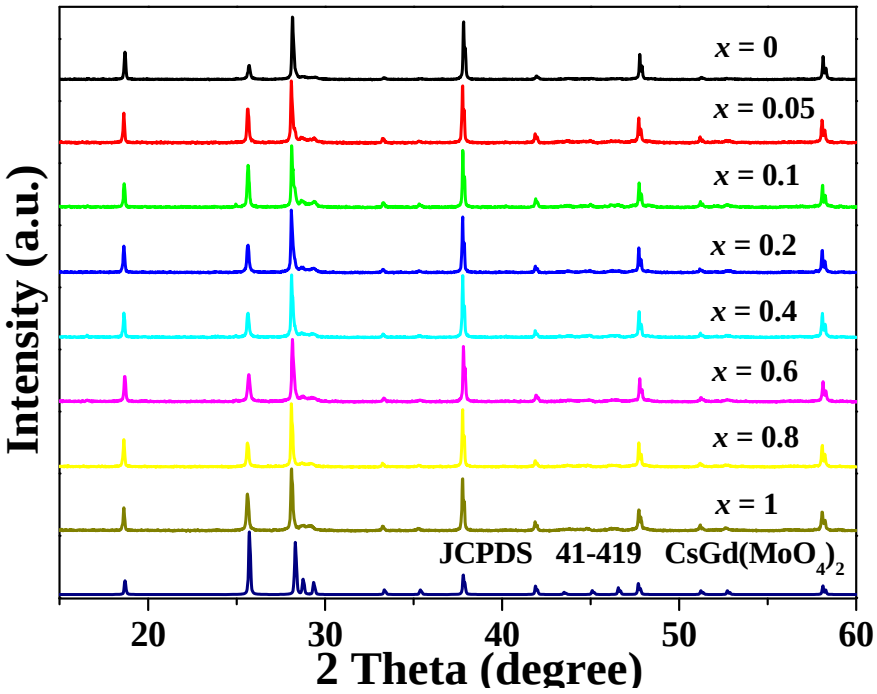

Fig. 1 XRD patterns of samples $CsGd_{1-x}Eu_x(MoO_4)_2$ (x = 0, 0.05, 0.10, 0.20, 0.40, 0.60, 0.80, 1.0) and JCPDS 49-419 $CsGd(MoO_4)_2$ as a reference.

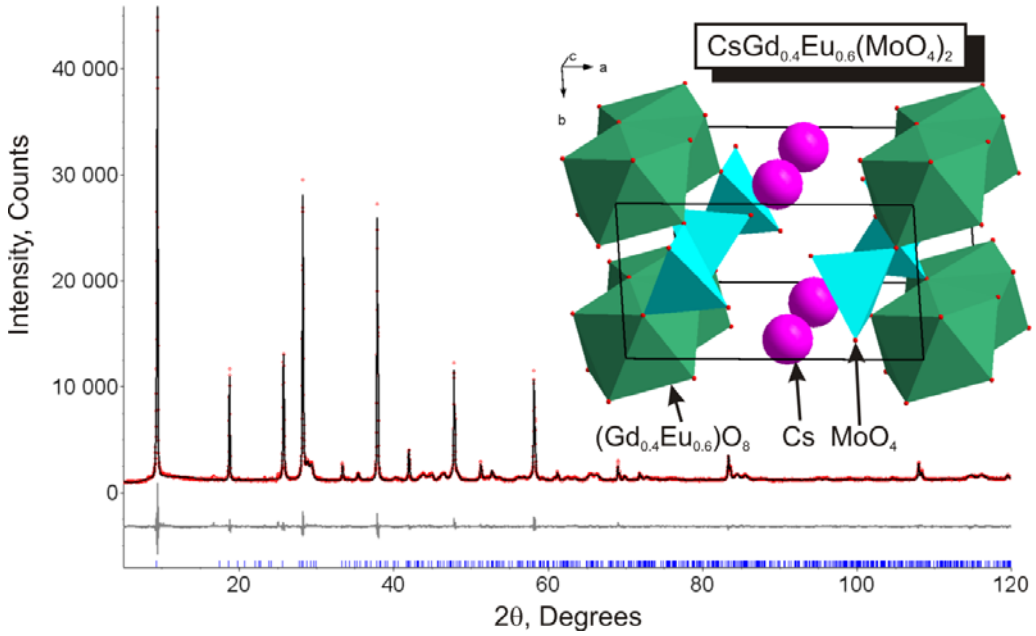

Fig. 2 Experimental and calculated XRD patterns, and Rietveld difference plot of $CsGd_{0.4}Eu_{0.6}(MoO_4)_2$ at room temperature. Inset shows crystal structure.

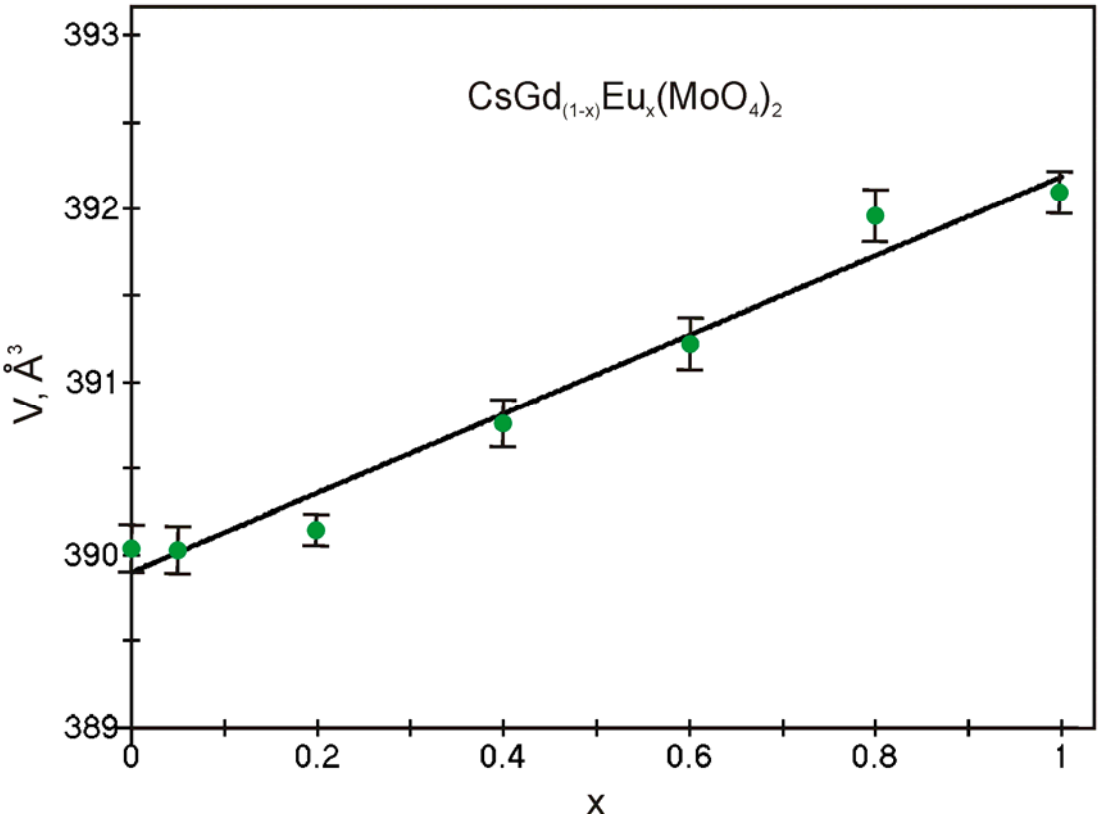

Fig. 3 Dependence of unit cell volume *V* on *x* in $CsGd_{(1-x)}Eu_x(MoO_4)_2$ molybdates.

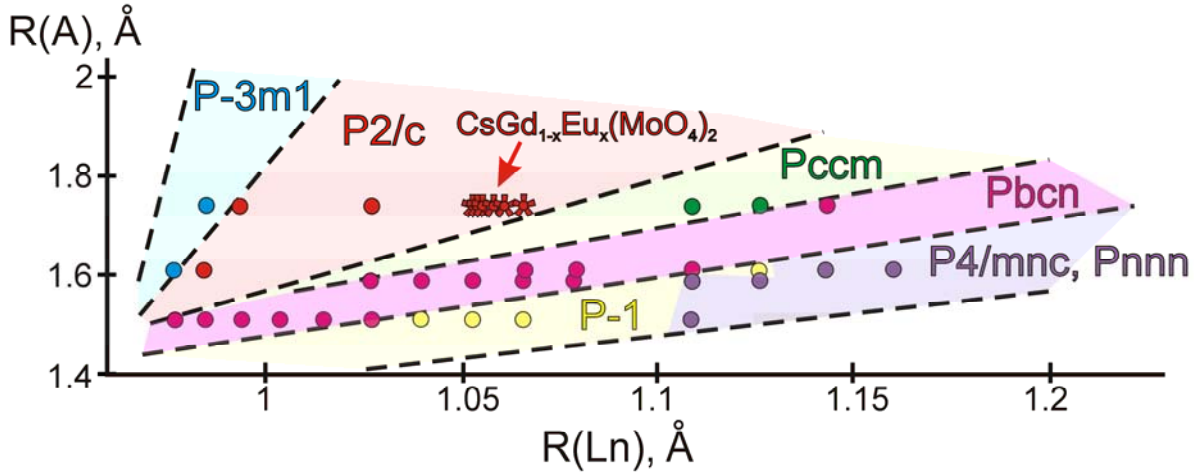

Fig. 4 Different structure fields in $ALn(MoO_4)_2$ (A = Li+, Na+, K+, Cu+, Rb+, Ag+, Cs+, Tl+) molybdates. $CsGd_{(1-x)}Eu_x(MoO_4)_2$ compounds are marked by arrow.

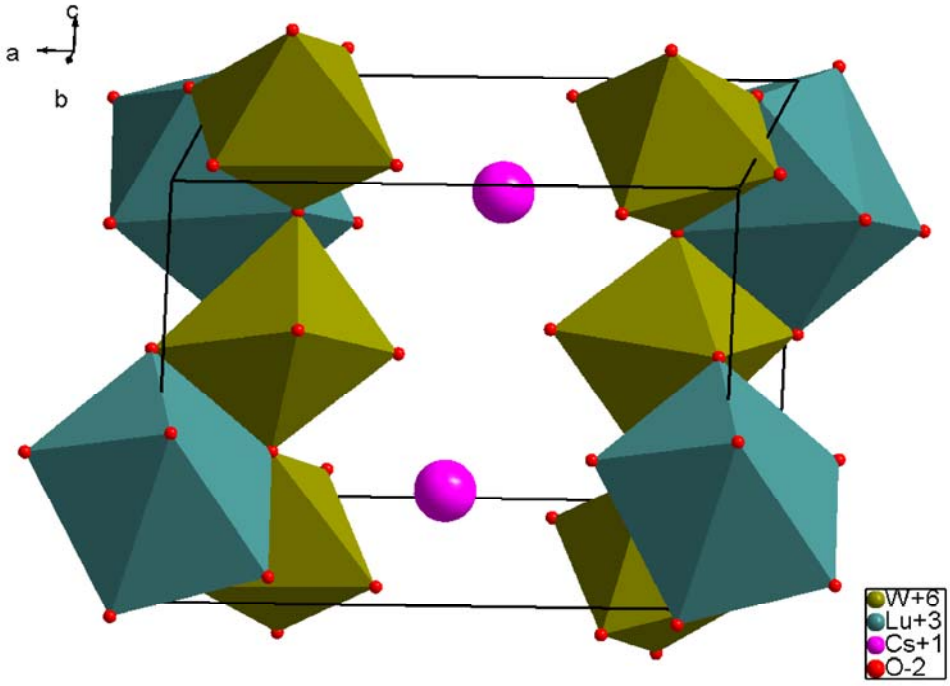

Fig. 5 Crystal structure of $CsLu(WO_4)_2$ with octahedrons WO_6.

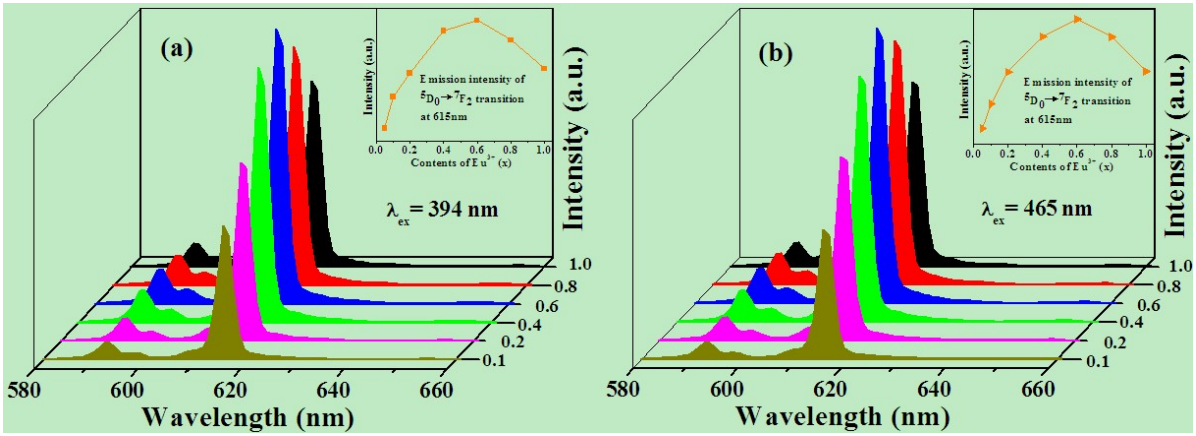

Fig. 6 PL spectra of samples $CsGd_{1-x}Eu_x(MoO_4)_2$ (x = 0.10, 0.20, 0.40, 0.60, 0.80, 1.0) at 394 nm (a), 465 nm (b) excitation, the inset shows the dependence of PL intensity on the Eu^{3+} doping concentration.

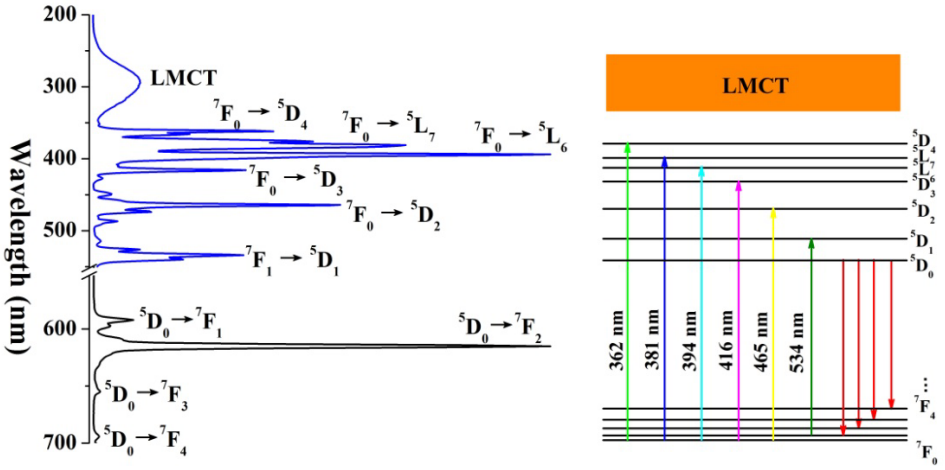

Fig. 7 PLE (λ_{em} = 615 nm, blue line) and PL (λ_{ex} = 394 nm, black line) spectra with energy level diagram of Eu^{3+} in $CsGd_{0.4}Eu_{0.6}(MoO_4)_2$ phosphor at RT.

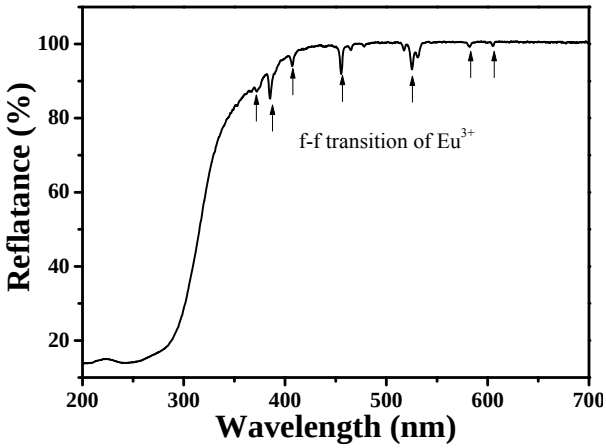

Fig. 8 UV-Vis reflectance spectrum of the $CsGd_{0.4}Eu_{0.6}(MoO_4)_2$ phosphor.

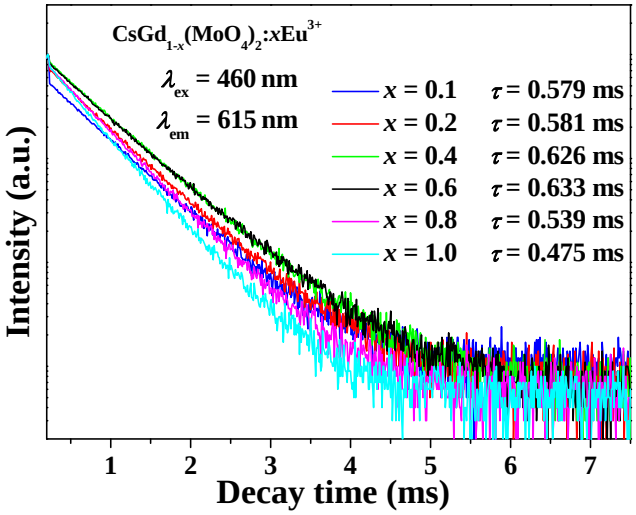

Fig. 9 The decay curves of samples $CsGd_{1-x}Eu_x(MoO_4)_2$ (x = 0.10, 0.20, 0.40, 0.60, 0.80, 1.0) at room temperature.

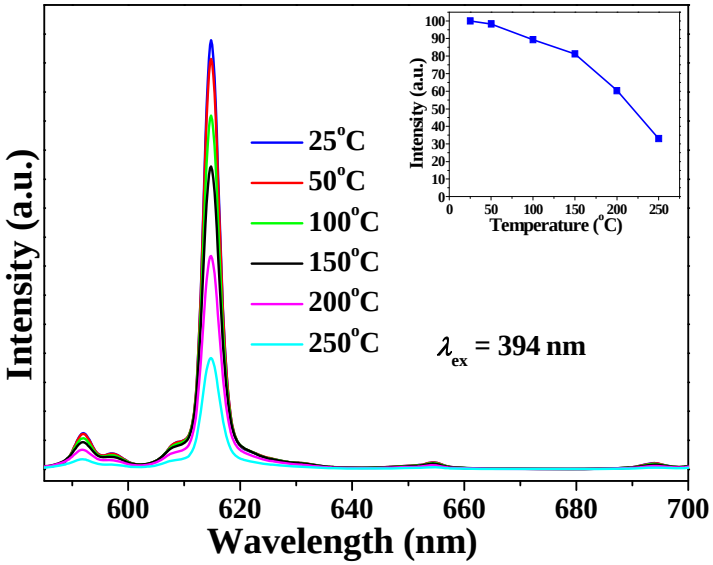

Fig. 10 The PL spectra (λ_{ex} = 394 nm) of $CsGd_{0.4}Eu_{0.6}(MoO_4)_2$ phosphor at different temperatures in the range of 25-250 ^{o}C. The inset shows the dependence of PL intensity on temperature.

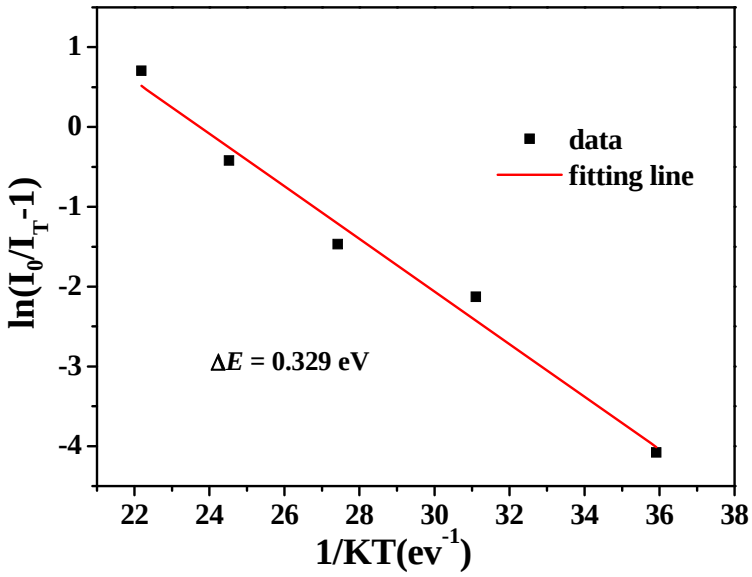

Fig. 11 A ln[(I_0/I_T)-1] *vs*. 1/*k*T activation energy graph for thermal quenching of $CsGd_{0.4}Eu_{0.6}(MoO_4)_2$ phosphor.

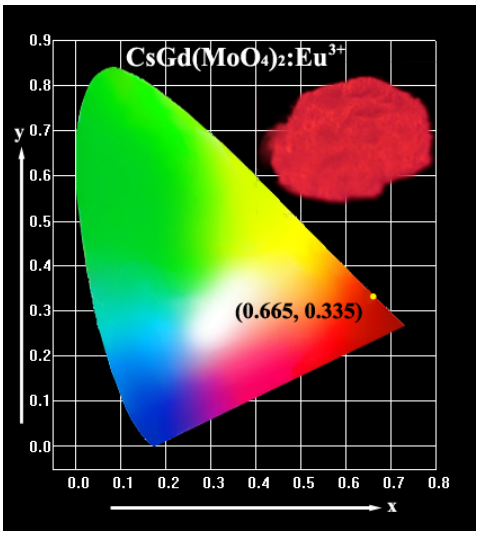

Fig. 12 The CIE chromaticity coordinate diagram of red phosphors $CsGd_{0.4}Eu_{0.6}(MoO_4)_2$.

Table 1. Main refinement parameters of $CsGd_{1-x}Eu_x(MoO_4)_2$ phosphors with different chemical compositions.

Formula	$CsEu(MoO_4)_2$	$CsGd_{0.2}Eu_{0.8}(MoO_4)_2$	$CsGd_{0.4}Eu_{0.6}(MoO_4)_2$	$CsGd_{0.6}Eu_{0.4}(MoO_4)_2$	$CsGd_{0.8}Eu_{0.2}(MoO_4)_2$	$CsGd(MoO_4)_2$
Space Group	*P2/c*					
Cell parameters	*a*=9.5255(1) Å *b*=5.0886(2) Å *c*=8.0901(1) Å *β*=90.868(6)º *V*=392.09(4) Å^3	*a*=9.5256(2) Å *b*=5.0884(2) Å *c*=8.0881(9) Å *β*=90.853(5)º *V*=391.97(5) Å^3	*a*=9.5247(1) Å *b*=5.0862(2) Å *c*=8.077(1) Å *β*=90.823(6)º *V*=391.22(5) Å^3	*a*=9.5264(2) Å *b*=5.0837(2) Å *c*=8.0702(8) Å *β*=91.085(6)º *V*=390.76(4) Å^3	*a*=9.5261(2) Å *b*=5.0810(2) Å *c*=8.0623(6) Å *β*=91.154(6)º *V*=390.15(3) Å^3	*a*=9.5289(2) Å *b*=5.0823(2) Å *c*=8.0563(7) Å *β*=91.246(6)º *V*=390.06(4) Å^3
D_x (g/cm^3), M_r	D_x = 5.122 M_r = 604.76	D_x = 5.133 M_r = 605.82	D_x = 5.152 M_r = 606.86	D_x = 5.167 M_r = 607.93	D_x = 5.184 M_r = 608.98	D_x = 5.194 M_r = 610.03
Number of reflections / Number of parameters	588 / 88	587 / 99	587 / 99	586 / 99	586 / 99	585 / 90
R-factors, %	R_{wp}= 4.59 R_p= 3.58 R_B= 1.28 R_{exp}= 2.60 χ^2= 1.77	R_{wp}= 4.11 R_p= 3.23 R_B= 0.92 R_{exp}= 2.50 χ^2= 1.64	R_{wp}= 4.41 R_p= 3.36 R_B= 1.02 R_{exp}= 2.49 χ^2= 1.77	R_{wp}= 4.39 R_p= 3.26 R_B= 1.19 R_{exp}= 2.58 χ^2= 1.70	R_{wp}= 3.90 R_p= 3.00 R_B= 0.82 R_{exp}= 2.49 χ^2= 1.56	R_{wp}= 4.56 R_p= 3.42 R_B= 1.39 R_{exp}= 2.41 χ^2= 1.89